atmosphere

Article

Assessing the Effects of Urban Canopy on Extreme Rainfall over the Lake Victoria Basin in East Africa Using the WRF Model

Joan Birungi [1,2,3], Jinhua Yu [1,2,*], Abdoul Aziz Saidou Chaibou [4], Nyasulu Matthews [5] and Emmanuel Yeboah [6]

1 Key Laboratory of Meteorological Disaster, Ministry of Education (KLME)/Collaborative Innovation Centre on Forecast and Evaluation of Meteorological Disasters (CIC-FEMD), Nanjing University of Information Science and Technology, Nanjing 210044, China; joan.birungi@unma.go.ug
2 School of Atmospheric Science, Nanjing University of Information Science and Technology, Nanjing 210044, China
3 Uganda National Meteorological Authority, Kampala P.O. Box 7025, Uganda
4 Département de Physique, Faculté des Sciences et Techniques, Université Abdou Moumouni, Niamey BP 10662, Niger; abdoulaziz.saidou@uam.edu.ne
5 School of Applied Meteorology, Nanjing University of Information Science and Technology, Nanjing 210044, China; 20215108001@nuist.edu.cn
6 School of Remote Sensing & Geomatics Engineering, Nanjing University of Information Science and Technology, Nanjing 210044, China; emmanuelyeboah@nuist.edu.cn
* Correspondence: jhyu@nuist.edu.cn

Abstract: The model simulation focuses on an extreme rainfall event that triggered a flood hazard in the Lake Victoria basin region of East Africa from June 24th to 26th, 2022. This study investigates the impacts of its urban canopy on the extreme rainfall events over the Lake Victoria basin in East Africa, employing the Weather Research and Forecasting (WRF) model at a convective-permitting resolution. The rapid urbanization of the region has given rise to an urban canopy, which has notable effects on local weather patterns, including the intensity and distribution of rainfall. The model incorporates high-resolution land use and urban canopy parameters to accurately capture the influences of urbanization on local weather patterns. This research comprises three sets of experiments, two with urban areas and one without, using the WRF model; the experiments focus on three days of an extreme rainfall event in the Lake Victoria basin. Satellite-based precipitation products and reanalysis datasets are employed for a synoptic analysis and model evaluation. The results demonstrate the model's effectiveness in capturing meteorological variables during an extreme event compared to observed data. The synoptic patterns reveal that, during the extreme event, the Mascarene and St. Helena influenced rainfall conditions over the Lake Victoria Basin by directing moist air toward the northwest. This led to increased moisture convergence from the urban–rural interface toward urban areas, enhancing convection and processes that result in extreme rainfall. Moreover, this study indicates that the urban canopy, specifically the building effect parameterization, significantly amplifies the intensity and duration of rainfall in the urban areas of the region. This research also indicates a general increase in air temperature, relative humidity, latent heat flux, and surface sensible heat flux due to the urban canopy. These findings highlight the substantial influence of urbanization on rainfall patterns in the urban environment.

Keywords: extreme rainfall; urban canopy; sensitivity test; WRF model

check for updates

Citation: Birungi, J.; Yu, J.; Chaibou, A.A.S.; Matthews, N.; Yeboah, E. Assessing the Effects of Urban Canopy on Extreme Rainfall over the Lake Victoria Basin in East Africa Using the WRF Model. *Atmosphere* **2024**, *15*, 226. https://doi.org/10.3390/atmos15020226

Academic Editors: Constanta-Emilia Boroneant, Bogdan Antonescu, Feifei Shen and Teodoro Georgiadis

Received: 24 December 2023
Revised: 23 January 2024
Accepted: 7 February 2024
Published: 14 February 2024

1. Introduction

The Lake Victoria basin (LVB) and its surrounding areas face susceptibility to extreme events, exemplified by destructive flash floods resulting from intense rainfall in mountainous regions [1,2]. In recent times, there has been rapid progress in the development of the urban canopy model (UCM) in conjunction with mesoscale models. [3] conducted a comprehensive review outlining the evolution and status of urban canopy schemes within the WRF model. This encompasses bulk urban parameterization (BULK) [4], a single-layer urban canopy model (SLUCM) [5], a multilayer urban canopy model (BEP) [6], and a simple building energy model (BEM) [7] linked to BEP. The WRF model, coupled with UCM (WRF/UCM), has been extensively utilized to explore the impacts of urbanization processes, such as the urban heat island effect and urban air quality.

Cities not only alter the permeability of surfaces and impact the extent of storms but also have the potential to amplify short-duration (sub-daily) extreme rainfall intensities [8,9], which are primary triggers for urban pluvial floods [10]. Several factors, including surface roughness, the presence of tall buildings, urban heat islands (UHI), heightened sensible heat, and aerosol concentration, can contribute to the intensification of extreme rainfall in urban areas [11,12]. The increase in surface roughness within a city compared to its surroundings is linked to the deceleration of air masses moving toward the city, leading to an augmented surface moisture convergence that elevates the rainfall intensity [13].

The urban environment plays a pivotal role in shaping meteorological conditions and radiation fluxes, especially during extreme weather events [14]. The impact of urbanization on weather patterns and energy balance has attracted heightened attention due to its far-reaching implications for public health, urban planning, and climate change. In the specific context of the Lake Victoria basin (LVB), an area marked by rapid urban expansion and susceptibility to intense rainfall events, it is of the utmost importance to understand the influence of an urban canopy on meteorological parameters [15–18].

An urban canopy, consisting of buildings, roads, vegetation, and other structures, possesses the capacity to influence local weather conditions via various mechanisms. Urban areas commonly display elevated temperatures in comparison to the surrounding rural areas, a phenomenon known as the urban heat island effect [19–21]. This temperature differential is attributed to factors such as diminished vegetation cover, expanded impervious surfaces, and the generation of anthropogenic heat. Consequently, extreme rainfall events in urbanized areas may interact with evolving meteorological conditions, potentially resulting in heightened rainfall intensity and modified storm dynamics.

Furthermore, the urban canopy can shape the formation and behavior of clouds [14,22]. The presence of tall buildings can serve as impediments to the vertical movement of air masses, giving rise to localized updrafts and downdrafts. These vertical motions contribute to enhanced cloud formation and precipitation processes, potentially leading to more pronounced rainfall in urban areas. A crucial facet of the urban canopy's impact on meteorology is its influence on radiation fluxes. Vegetation plays a pivotal role in regulating the energy exchange between the land surface and the atmosphere through processes such as evapotranspiration, solar radiation absorption, and reflection. As urban areas undergo a reduction in vegetation cover and an increase in artificial surfaces, significant changes occur in the energy balance and radiation budget. These alterations can give rise to shifts in local temperature patterns, atmospheric stability, and the formation and intensity of rainfall systems [9,23].

The LVB, which includes rapidly growing urban centers such as Kampala, Nairobi, and Kisumu, is undergoing swift urbanization, population expansion, and changes in land use [24,25]. These dynamics have the potential to exacerbate the consequences of extreme rainfall events, leading to heightened flood risks, damage to infrastructure, and threats to human lives and livelihoods. Consequently, it is imperative to conduct a comprehensive investigation into how the urban canopy in this region interacts with meteorological conditions during extreme rainfall events.

Gaining a nuanced understanding of the intricate relationship between urbanization and meteorology in the LVB can offer valuable insight for urban planners, policymakers, and disaster management agencies. By pinpointing the specific mechanisms through which the urban canopy influences extreme rainfall, strategies can be formulated to mitigate the adverse impacts of such events and bolster urban resilience. Furthermore, this research contributes to a broader understanding of the urban environment's role in local and regional climate dynamics, facilitating efforts to address the challenges posed by urbanization and climate change.

This study aims to examine the impact of the urban canopy on meteorological conditions during an extreme rainfall event in the Lake Victoria basin (LVB). We set out to evaluate the spatiotemporal variations in rainfall characteristics and other meteorological parameters across urban and rural areas, employing a combination of observational data, numerical modeling, and statistical analyses. The outcomes of this investigation contribute to a more holistic understanding of the interaction between urban environments and the atmosphere, offering valuable insight for sustainable urban planning and climate resilience in the LVB and analogous regions experiencing rapid urbanization and extreme weather events.

The remainder of the paper is organized as follows: Section 2 provides details on the study area, data, and methodology employed, while Section 3 examines the findings. Finally, Section 4 outlines the primary conclusions derived from the study.

2. Materials and Methods

2.1. Study Area and Selection of the Heavy Rainfall Event

The basin encompasses portions of Burundi, Rwanda, Kenya, Tanzania, and Uganda, as depicted in Figure 1. Positioned within a continental sag between the two arms of the Great Rift Valley system, the basin is flanked by elevated mountain ranges to the east and west, including Kilimanjaro, Kenya, and Rwenzori. The altitude of the lake surface is approximately 1135 m above the mean sea level, while the basin itself comprises a succession of stepped plateaus with an average elevation of 2700 m, rising to 4000 m or more in the highland areas [26]. The land use and land cover in the LVB have undergone significant transformations, primarily due to human activities resulting in the conversion of forests, woodlands, grasslands, and wetlands into either agricultural land or settlements [27]. Figure 1 depicts the changes of land use/land cover up to the year 2022, utilizing Landsat multi-temporal satellite images. The Lake Victoria region stands out as one of the most densely populated areas in East Africa, boasting a population exceeding 30 million [5,28,29].

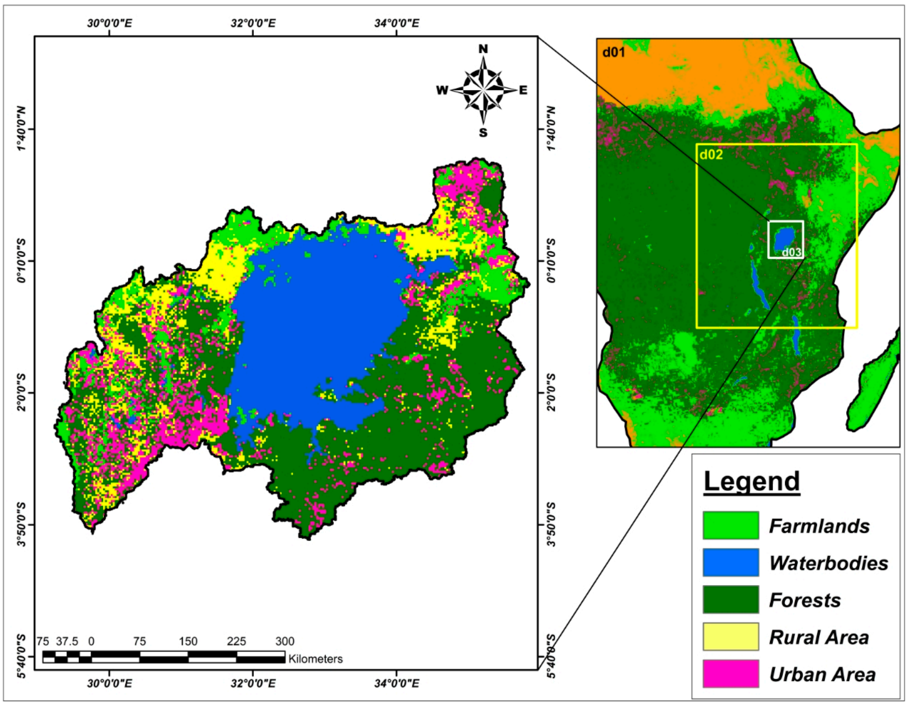

Figure 1. The simulated domain is shown on the right within the location of the Lake Victoria basin, showing land-use-category data from WRF model simulations for the year 2022.

The definition of severe rainfall used in this study is taken from the World Meteorological Organization (WMO)'s Severe Weather Forecasting Programme (SWFP). According to SWFP, the threshold for defining severe rainfall is set at 50 mm [30]. Table 1 presents rainfall data, specifically noting instances of more than 20 mm recorded in the Lake Victoria basin between the 24th and 26th of April 2022. A 20 mm threshold is chosen on the basis that it becomes extreme if experienced persistently in the region for more than two consecutive days (https://community.wmo.int/en/activity-areas/severe-weather-forecasting-programme-swfp, accessed on 22 March 2022).

Table 1. The rainfall reported on the 24th, 25th, and 26th of April around the Lake Victoria basin with levels above 20 mm.

Date	Stations	Rainfall (mm)
24 April 2022	Bukoba (Tanzania)	74.6
	Kisumu Met (Kenya)	48.7
	Kampala (Uganda)	29.5
	Entebbe (Uganda)	29.3
	Nyahururu (Kenya)	28
	Narok Met. (Kenya)	25.9
	Nyakibanda (Rwanda)	25.3
	Rubona (Rwanda)	21.5
25 April 2022	Shinyanga (Tanzania)	31.3
26 April 2022	Ukiriguru Met. (Tanzania)	137
	Nyakibanda (Rwanda)	62.1
	Kibeho (Rwanda)	45.7
	Bukoba (Tanzania)	40.3
	Jinja (Uganda)	35.2
	Mwanza (Tanzania)	35.1
	Kinigi (Rwanda)	31.4
	Byumba (Rwanda)	30
	Kigali (Rwanda)	24.4
	Nyagahanga (Rwanda)	23.8

2.2. The Interactions between Lake Victoria and the Atmosphere

The storms in this region are caused by circulation in the atmosphere above Lake Victoria. Daytime breezes flow outward from the relatively cool surface of the lake toward the sunbaked land. At night, the pattern reverses, and land breezes converge over the water. Combined with evaporation from the vast lake and warm-air convection into the atmosphere, this results in thunderstorms [31].

The lake's large surface area and relatively warm temperatures can lead to the evaporation of water into the atmosphere. This process contributes to the moisture content in the air, which can then lead to precipitation in the form of rain or storms in the surrounding region [32].

Additionally, the presence of Lake Victoria also influences local wind patterns. The temperature difference between the lake and the surrounding land can create a temperature gradient, leading to the formation of breezes or winds that can affect the local climate and weather patterns [33].

The lake also plays a role in regulating the temperature of the surrounding area. During the day, the water in the lake absorbs heat from the sun, helping to moderate the temperature of the air above it. At night, the lake releases this heat, keeping the surrounding area warmer than it would be otherwise [34].

In summary, the interactions between Lake Victoria and the atmosphere are complex and dynamic, with the lake exerting a significant influence on the local climate and weather patterns in the region.

2.3. Model Description and Experiments

The Weather Research and Forecasting model, version 4.4.2, with a convective-permitting resolution of 3 km, was employed to simulate the impact of the urban canopy on meteorology during an extreme rainfall event in the LVB [35]. The model runs were conducted using a modified version of WRF, specifically version 4.4.2. The WRF model is a non-hydrostatic compressible model that utilizes a mass coordinate system, and it is widely used as a mesoscale meteorological model. The version utilized in this study incorporates an updated urban Local Climate Zone (LCZ) numbering system, ranging from 51 to 61 in parameter tables, to prevent potential overlaps with existing land-type data.

The simulation period commenced on 23 April 2022 at 00:00 UTC and lasted until 26 April 2022, 00:00 UTC. To ensure the model's stability, the first day (24 h) of the output was designated as spin-up time, with the subsequent 96 h considered for analysis. The initial and boundary conditions for the simulations were derived from the European Centre for Medium-Range Weather Forecasts (ECMWF) ERA5 reanalysis datasets, obtained from the NCAR/UCAR website (rda.ucar.edu); these datasets feature a horizontal resolution of 0.25°.

Three experiments were conducted during this study. The first experiment involved replacing urban areas with the dominant surrounding vegetation category (referred to as non-urban physics or non-urban). The other two experiments served as control simulations and utilized the default land use of two distinct urban physics schemes, which included urban areas. The model was executed with three nested domains as shown in Table 2., featuring horizontal resolutions of 27 km, 9 km, and 3 km, and encompassing 50 vertical levels from the surface to the 50 hPa level. The investigation into the effects of the urban canopy was carried out by analyzing the differences between the control simulations and the non-urban simulation.

Table 2. Model configuration and scheme setting.

	D01	**D02**	**D03**
Model		WRF-ARW V.4.4.2	
Grid spacing (km)	27	9	3
Radiation		RRTMG	
Land surface model	Noah-LSM +single-layer UCM+ building effect parameterization (BEP)		
PBL		BouLac boundary layer scheme	
Cumulus parameterization	Grell 3D (5)	Grell 3D (5)	None

The control simulations involved the urban canopy model (UCM) three-category option with surface effects for roofs, walls, and streets. This included an experiment with a green roof option and utilized the PBL Yonsei University scheme: a non-local-K scheme with an explicit entrainment layer and a parabolic K profile in the unstable mixed layer (bl_pbl_physics = 1). Additionally, it incorporated building effect parameterization (BEP) with the PBL scheme BouLac PBL (8), i.e., Bougeault–Lacarrère PBL, which was specifically designed for use with the BEPurban model [36]. This scheme included a TKE prediction option.

Several physical parameterizations were switched on for this study, including the following:

1. The Noah-land-surface model [37], which was used to represent land-surface processes.
2. The rapid radiative transfer model (RRTMG) scheme for long- and short-wave radiation [38]. A radiative transfer model simulates the interaction of radiation with the atmosphere.
3. A modified MM5 surface layer scheme [39], which was employed for surface layer processes.
4. The BouLac boundary layer scheme [36], which was used to model boundary layer processes.
5. The Stony Brook University (Y. Lin) scheme [40]. A five-class scheme with riming intensity, which accounts for mixed-phase processes in microphysics.

Additionally, the cumulus convection scheme used in this study was the Grell 3D cumulus scheme [41] for domains d01 and d02. However, it was not used for the finest domain (d03), since the model can explicitly solve convection at such a fine resolution (3 km).

Figure 2 shows the systematic approach or set of procedures used to conduct research, in our case it involves a combination of data analysis, numerical modeling, and scientific interpretation to assess the effects of the urban canopy on extreme rainfall and other weather parameters using the WRF model.

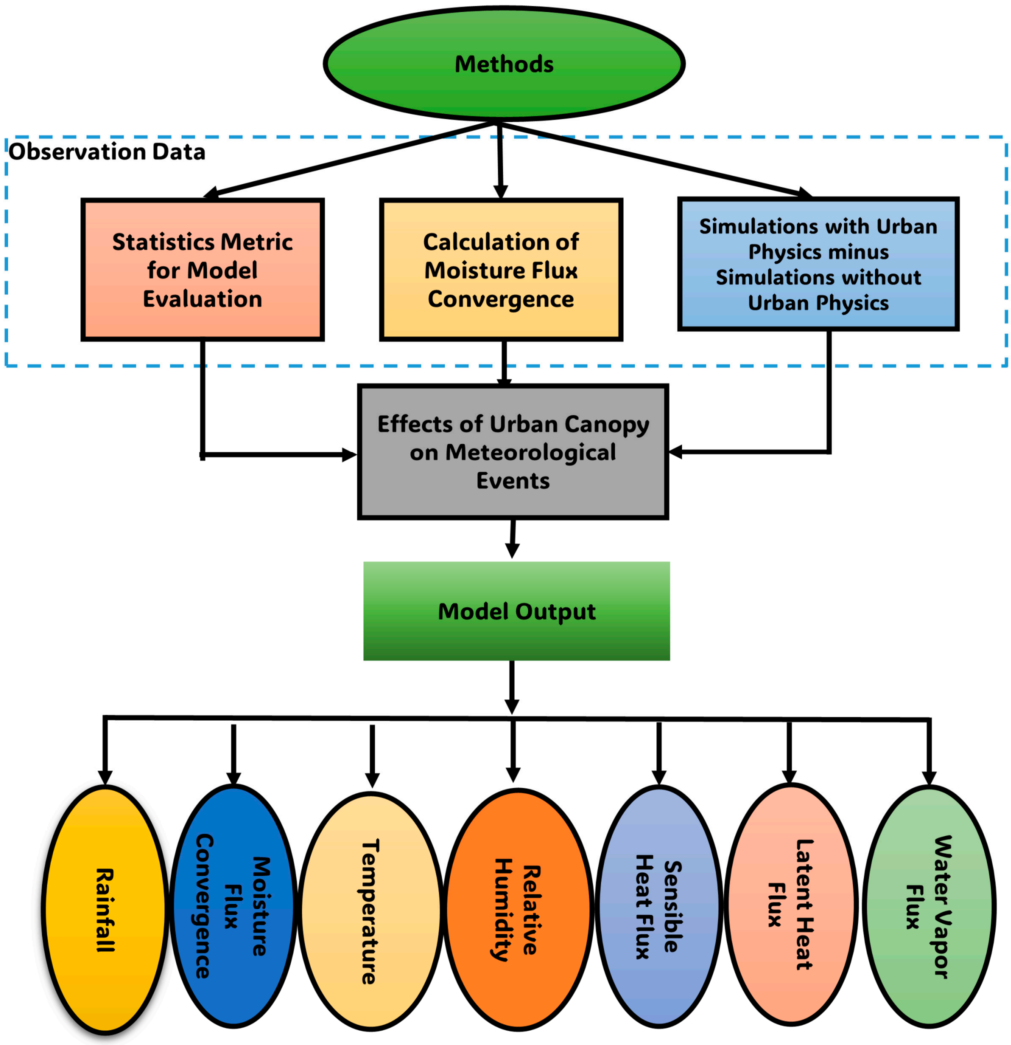

Figure 2. Study methodology.

2.4. Observational Data

The satellite-based precipitation data utilized in this study are derived using the Climate Prediction Centre (CPC)'s morphing technique (CMORPH), which comprises global high-resolution satellite precipitation estimates [42]. The dataset has undergone bias correction and reprocessing. Initially, global precipitation data taken solely from satellites are integrated, drawing from all available passive microwave measurements aboard low-Earth orbiting platforms. To rectify biases, these integrated precipitation data are compared with the CPC daily gauge analysis over land and the Global Precipitation Climatology Project (GPCP) analyses conducted over the ocean [43]. The CMORPH data are then reprocessed on a global grid with a spacing of 8 km $\times$ 8 km and a temporal interval of 30 min, covering the period from January 1998 to the present. This dataset has previously been employed in studies focusing on the rainfall climate in cities and in numerical modeling evaluations [44–46]. In specific instances related to Africa, the daily data are downscaled to a spatial resolution of 0.25° $\times$ 0.25°. This reduction in the spatial resolution is undertaken to facilitate and enhance support for land-surface modeling activities. Downscaling allows for a more detailed representation of geographical features and local conditions, providing valuable input for land-surface models operating at a finer scale.

ERA5, on the other hand, constitutes the fifth-generation ECMWF reanalysis, providing global climate and weather data for the past eight decades [47,48]. The data are available from 1940 onward, replacing the ERA-Interim reanalysis. ERA5 offers hourly estimates for various atmospheric, ocean-wave, and land-surface quantities.

2.5. Statistical Metrics for Model Evaluation

The predominant approach for assessing the model involves employing statistical analysis with observed data. While the evaluation process aligns with validation methodologies in several respects, its primary objective is to gauge the model's capacity to replicate observed phenomena. The utilized statistical indices are shown in Appendix A, and the contingency table was formulated as shown in Table 3. Below.

Table 3. Contingency table derived from WRF rain availability and observations.

Contingency Table			
	OBS YES	**OBS NO**	
WRF/RAIN YES	Hits (HH)	False alarms (FAs)	Total events forecast
WRF/RAIN NO	Missed events (MMs)	Correct negatives (CNs)	Total non-events forecast
	Total events observed	Total non-events observed	Sample size

2.6. Calculation of the Moisture-Flux Convergence

Regarding the vertically integrated moisture-flux convergence (VIMFC), we define VIMFC as the horizontal moisture-flux convergence integrated between 1000 hPa and 500 hPa to measure the lower tropospheric forced lifting, as most water vapor exists below 500 hPa, i.e., as shown in Appendix A.

2.7. Observation Minus Reanalysis Method

The "observation minus reanalysis" (OMR) method is a valuable technique employed in meteorology and climate science to evaluate the precision and reliability of atmospheric observations, particularly within the realms of climate research and numerical weather predictions [49,50]. The widely used OMR method serves to explore the influence of urbanization and land-use changes on climate dynamics [51].

In the context of this study, simulations without urban physics (non-urban) were utilized as the control simulation. This was because we aimed to investigate the impact of the urban canopy on extreme weather events and radiation fluxes, providing insight into the effects of urbanization on these climatic factors.

3. Results and Discussion

3.1. Simulation of Rainfall Intensity and Related Factors in a Control Experiment

3.1.1. Rainfall distribution

Figure 3 depicts the spatial distribution of a rainfall event occurring between the 24th and 25th of April 2022. Initially, the observation data from CMORPH and the two control experiments (denoted as b and c) exhibited a comparable pattern, indicating substantial precipitation over the lake and the western regions of the study domain. Nevertheless, we observed that, when compared to simulations with the urban canopy (urban), the simulations incorporating the building effect parameterization demonstrated a more dispersed rainfall pattern. Urban areas often experience higher temperatures than surrounding rural areas due to the urban heat island effect. This localized warming is caused by the concentration of buildings, pavements, and other heat-absorbing materials [52]. The higher temperatures can lead to increased atmospheric instability, which can enhance convective processes and potentially lead to more localized rainfall.

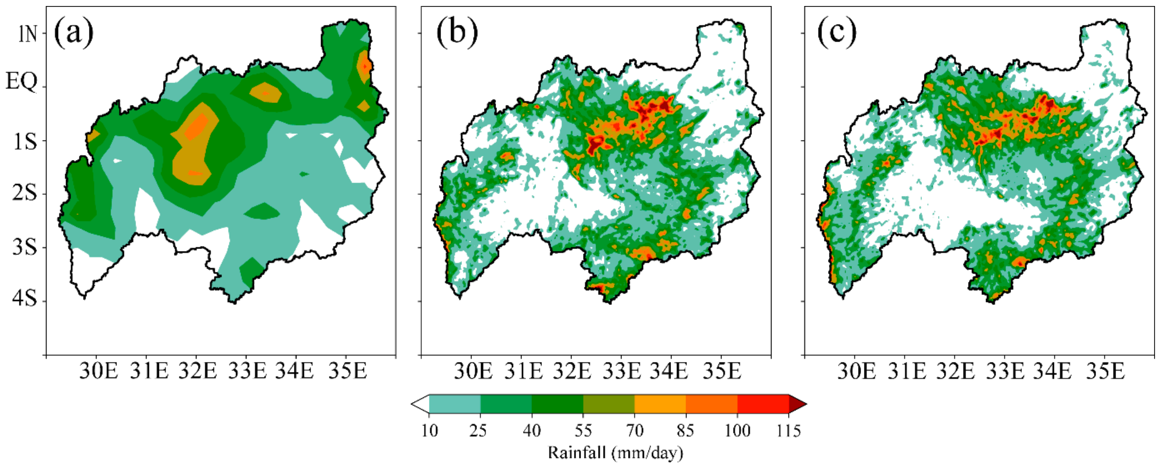

Figure 3. Spatial distribution of rainfall of the observation data: (**a**) CMORPH and the control simulations; (**b**) urban; and (**c**) BEPurban.

3.1.2. Diurnal Variation

Figure 4 illustrates the diurnal variation in the study area, showing elevated rainfall during the daytime on the 25th and 26th and during the nighttime on the 24th. Notably, the pattern was not consistent, suggesting that factors other than changes in the urban environment influence extreme rainfall. The study indicated that the urban building effect parameterization (BEP) tended to overestimate the maximum rainfall during the night while underestimating it during the day.

An inconsistent diurnal pattern was identified, with high levels of rainfall observed during the night extending into the daytime; meanwhile, on the 25th and 26th, high levels of rainfall were predominantly observed during the daytime. During the day, urban areas tend to experience the urban heat island effect, where temperatures are higher than in the surrounding rural areas. This localized warming can lead to increased atmospheric instability, which, in turn, can enhance convective processes and potentially lead to more localized rainfall during the day. Daytime heating from solar radiation can also lead to the development of thermal and local circulations within urban areas. These processes can contribute to the lifting of air and the formation of clouds, potentially leading to increased rainfall during the day. Anthropogenic heat sources contribute to the release of heat into the atmosphere. These anthropogenic heat sources can further enhance the urban heat island effect and contribute to increased convective activity and rainfall during the day [53,54]. This variation suggests that meteorological factors beyond changes in experimental physics may influence the diurnal pattern.

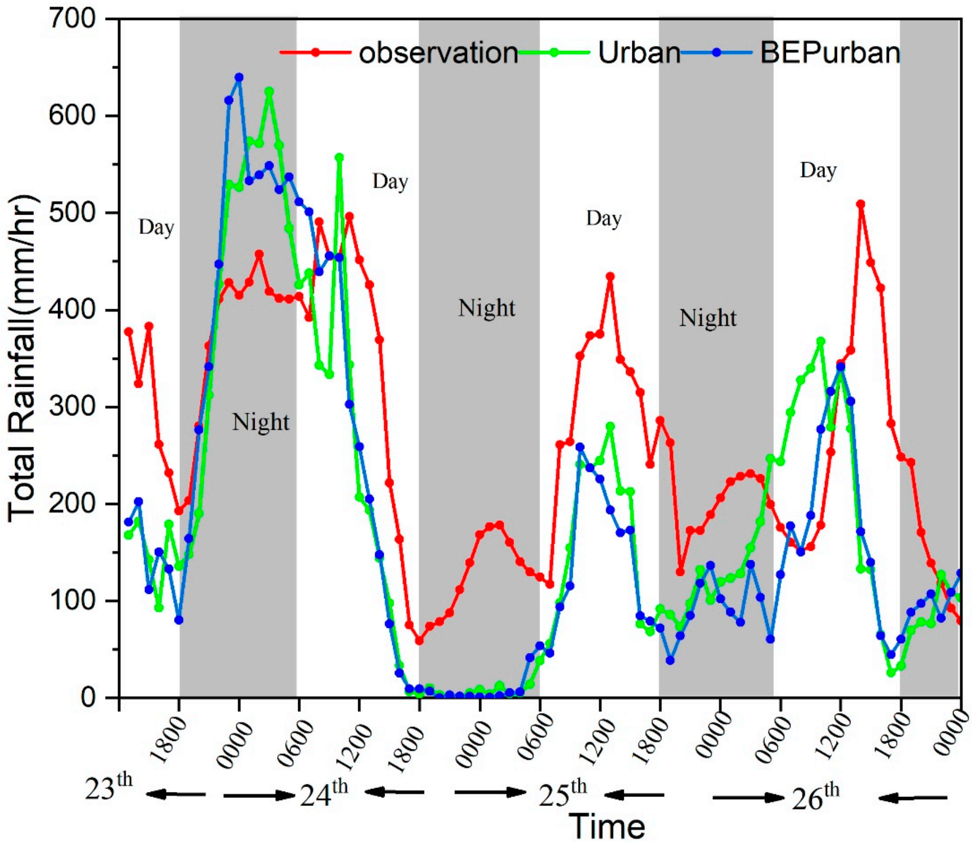

Figure 4. The diurnal cycle of the average spatial rainfall over the Lake Victoria basin for the observation (CMORPH) and the control experiments with the urban canopy models (urban and BEPurban).

3.2. Evaluation of the Model

Low bias, a small normalized root mean square error (NRMSE), and a higher positive correlation coefficient (CC) are generally indicative of a well-performing model [55]. The model's performance is evaluated by comparing the simulated results with the satellite product CMORPH. The initiation and evolution of rainfall over the Lake Victoria basin are tracked and compared between CMORPH and the simulations. To objectively assess the evolution of the extreme rainfall event in time and space, we utilize bias, the RMSE, and Pearson correlation coefficients to compare the two datasets. In the evaluation, we employ the Grell 3D cumulus scheme in the mother and second domains, considering its dualistic performance and relevance to the experiments [41]. The rain event is reproduced using CMORPH data, taking into consideration the fact that rainfall modeling is highly sensitive to the initial conditions, especially for short simulation periods to the scale of days. It is widely understood that, in numerical weather forecasting, the initial conditions (particularly the amount and instability of moisture) significantly impact the outcomes.

We evaluated the model's spatial capacity to replicate rainfall patterns across the Lake Victoria basin, and the outcomes are presented in a visual form in Figure 2. The analysis reveals that the WRF model exhibits a robust performance when compared to the observed datasets (CMORPH). Figure 5a,b illustrates the RMSE of the model within the study region, while (c, and d) depict the model's bias outcomes for the same area. The model tends to overestimate rainfall in the Lake Victoria area and underestimate it in the corresponding regions. The instances of the model overestimating precipitation in specific areas are highlighted. Specifically, high-positive-bias values (bias > 25 mm) are identified over Lake Victoria and certain western regions, while lower bias values (bias < −25 mm) are observed elsewhere.

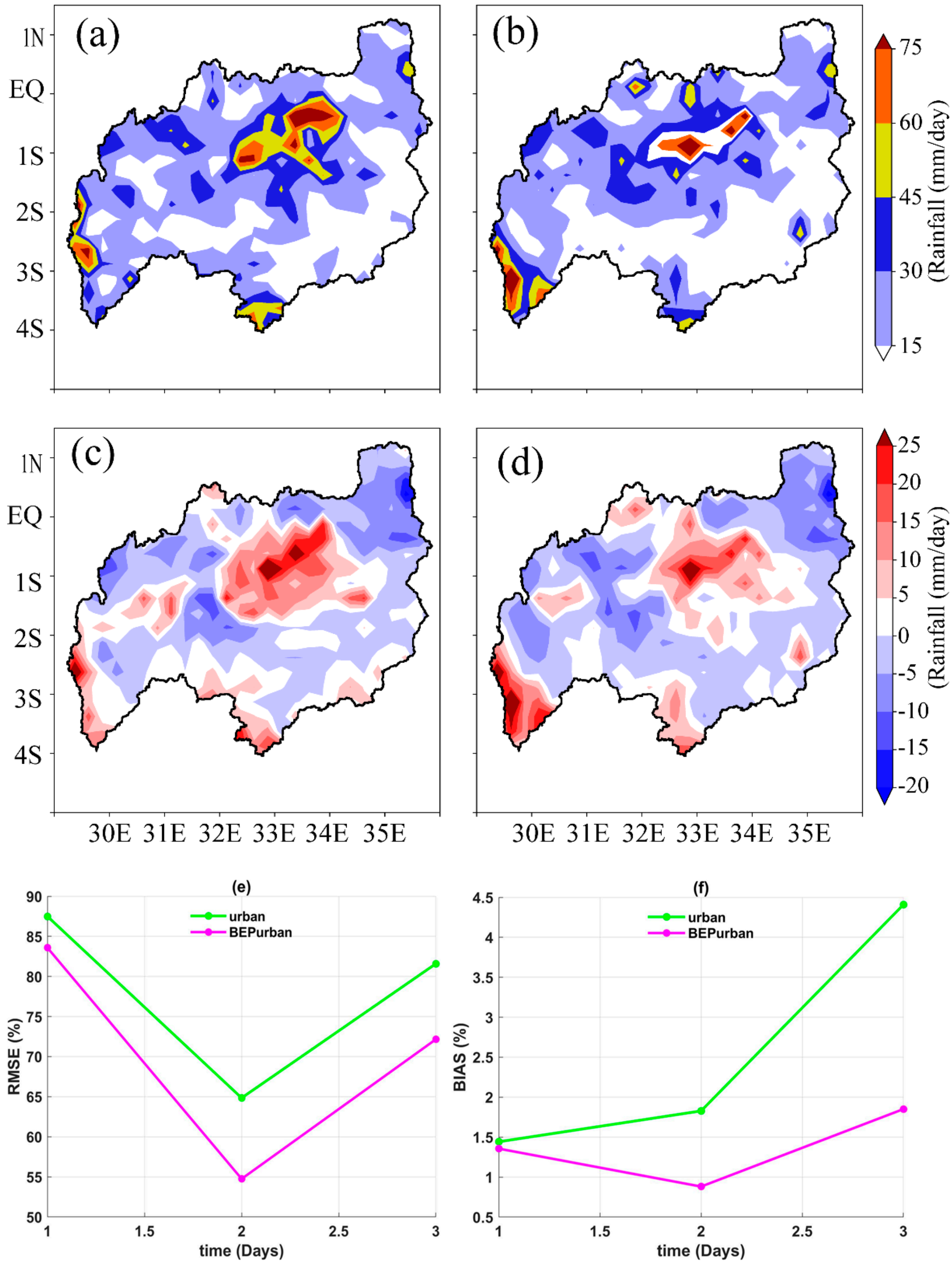

Figure 5. Spatially distributed bias and RMSE of the simulated rainfall: (**a**,**c**) bias, RMSE for UCM (urban canopy model)and (**b**,**d**) bias, RMSE for BEP–urban and time series, and (**e**) RMSE and (**f**) Bias.

The bias and RMSE during the rainfall event were further analyzed using time series analysis, and the results are presented in Figure 5e,f. The findings indicate that BEPurban outperformed non-urban and urban in terms of bias and RMSE in the rainfall time series analysis. Bias measures the systematic error in the model's predictions, indicating whether the model consistently overestimates or underestimates the observed values. A lower bias value for BEPurban indicates that the model's predictions are closer to the true values on average, with less systematic deviation. A lower bias value indicates that the model's average predictions are more accurate and closer to the true values, which is a positive indicator of the model's performance [56]. The RMSE measures the average magnitude of the errors between the predicted values and the observed values [57]. A lower RMSE for BEPurban indicates that the model's predictions are closer to the observed data points on average. In other words, the model's simulations are more accurate and exhibit smaller deviations from the actual data. This result also indicates that the model is better at capturing the variability and patterns in the observed data, which is a positive indicator of the model's performance.

The correlation of our model's simulation of the rainfall event using the CMORPH dataset in Figure 6a,b illustrates the relationship between the predicted values generated from the model and the actual values in a scattered plot and regression line. It measures the strength and direction of the linear relationship between the predicted and actual values for non-urban, urban, and BEPurban, with correlation coefficients of R = 0.7984, 0.78, and 0.83, respectively. In this context, our evaluation model, which showed a higher correlation, reveals that the BEPurban results exhibited a strong linear relationship between the simulated data and the observed data. This constitutes a strong positive indicator of the model's performance and its ability to simulate the behavior of the extreme rainfall being studied [58].

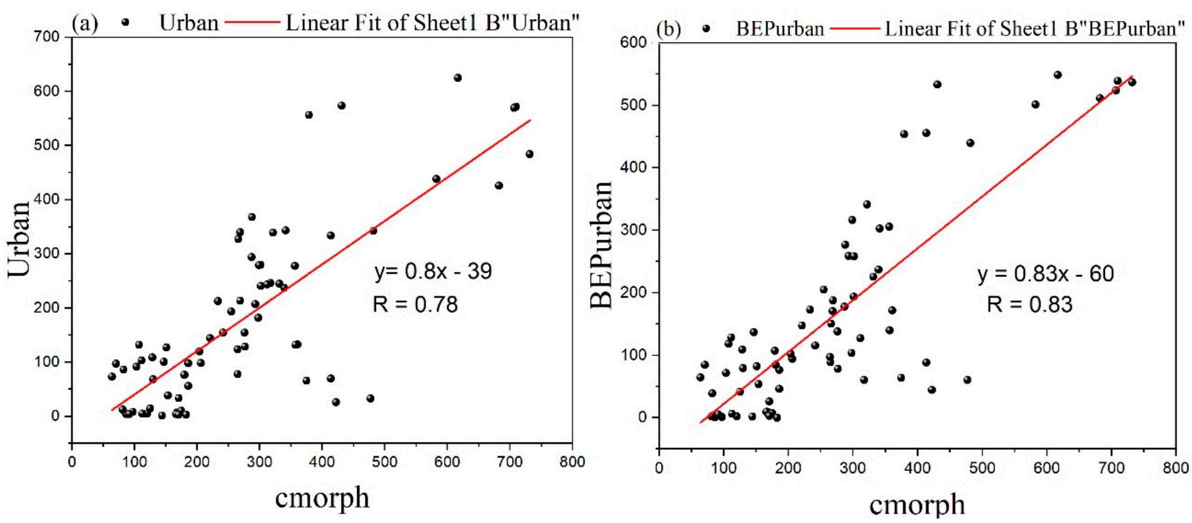

Figure 6. Scatter plot showing the correlation coefficient results between the control simulations (urban and BEPurban) and the observations (CMORPH dataset) (**a**) represents the Urban and (**b**) is the BEP–urban.

To realistically compare the model's performance against observations, we added more statistics, such as the false alarm ratio (FAR), the frequency bias index (FBI), the probability of detection (POD), and the critical success index (CSI) for the amount of rainfall experienced in the region, as shown in Table 4. The results of the two control experiments, the urban canopy model (urban), and the multiple-canopy model of building effect parameterization (BEPurban) show higher scores for POD, FBI, and CSI, along with a lower FAR score. This indicates that the WRF model exhibited a better spatial performance than CMORPH rainfall.

Table 4. Statistics related to the performance of the model for rainfall during the extreme event.

Score	Urban			BEPurban		
	24th	**25th**	**26th**	**24th**	**25th**	**26th**
False alarm ratio (FAR)	0.01	0.11	0.05	0.01	0.12	0.04
Frequency bias index (FBI)	0.99	1.03	1.01	1.00	1.02	1.03
Probability of detection (POD)	0.98	0.92	0.96	0.99	0.90	0.98
Critical success index (CSI)	0.97	0.83	0.92	0.98	0.80	0.94

The FBI index for the three experiments is one or almost equal to one, suggesting that the WRF model's results are spatially well-located compared to CMORPH rainfall. However, for the two experiments, BEPurban performed better than urban on days when there was extreme rainfall.

3.3. Effect of the Urban Canopy on Meteorology

3.3.1. Rainfall

To better understand the differences between the simulated experiments, a further analysis was conducted using the differences in simulated rainfall, as is shown in Figure 7. It can be observed that BEPurban has more significant modifications, especially over the lake and western locations. This implies that buildings have a more pronounced impact on the intensity of rainfall over the study domain. Generally, in urban locations, there is an urban thermal effect, whereby the heat from buildings can directly reinforce convective processes by attracting and converging moisture from the surrounding area, consequently enhancing extreme rainfall events over urban areas [59–61]. Changes in the surface runoff can lead to increased surface runoff and the reduced infiltration of water into the soil. As a result, less water is available for groundwater recharging and natural moisture storage, potentially affecting the availability of water for sustaining local ecosystems and contributing to rainfall patterns.

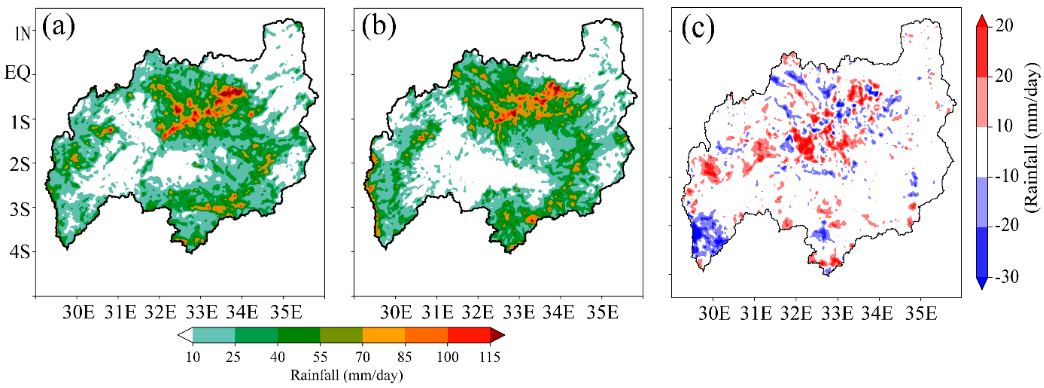

Figure 7. Rainfall simulations from the model, where (**a**) represents the simulation without urban physics (non-urban), (**b**) represents the simulation with building effect parameterization (BEP–urban), and (**c**) shows the comparison between the non-urban simulation (non-urban) and the control BEPurban (non-urban–BEPurban).

3.3.2. Moisture-Flux Convergence (MFC)

Figure 8 displays the vertically integrated moisture flux and wind fields. A noticeable contrast is observed in the non-urban and BEPurban simulations, indicating that strong convergence is induced by the urban canopy over the urban–rural interface. In comparison to the non-urban simulations, the BEP simulations exhibit enhanced convection over urban areas. This enhanced convection is mainly attributed to increased surface roughness over urban areas, which decelerates wind speeds and leads to the expansion of the convergence zone from the urban–rural interface toward the urban areas [19–21].

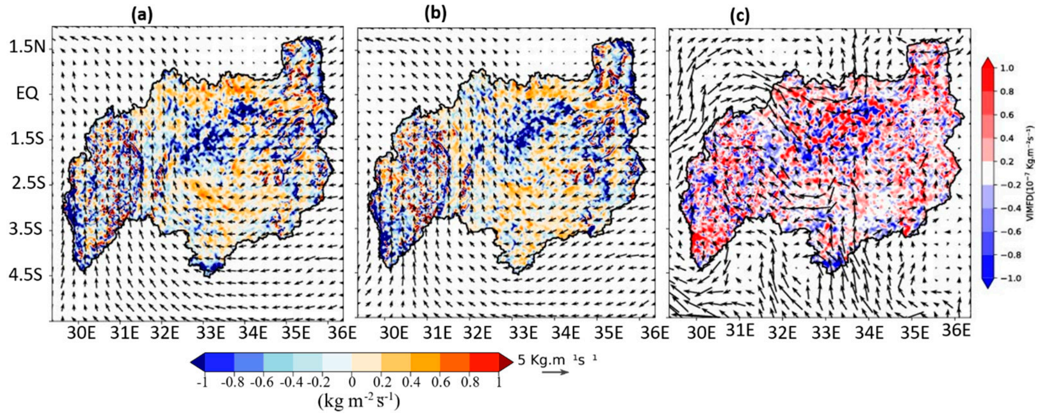

Figure 8. Shows the moisture convergence from (**a**) non-urban areas and the control simulation; (**b**) BEPurban; and (**c**) the difference between the non-urban experiments and the control simulations (non-urban–BEPurban).

3.3.3. Temperature

Figure 9 shows the spatial distribution of temperature across two meters during the extreme rainfall event (a, b, and c), along with the difference between the non-urban simulation and the control experiment (BEPurban). The simulated temperature in all environments, both non-urban and BEPurban, indicates an increase in temperature over the lake and a decrease as one moves further away from the lake.

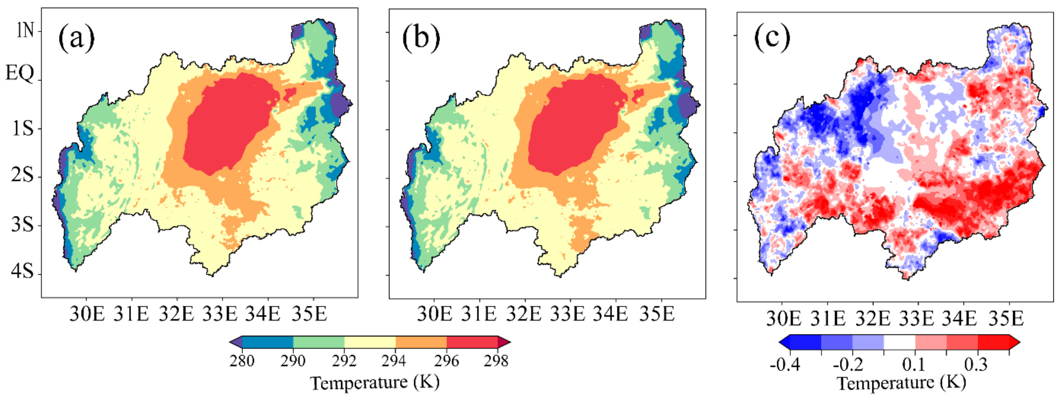

Figure 9. Spatially distributed 2 m temperature: (**a**) non-urban, (**b**) control (BEPurban), and (**c**) the difference between the non-urban experiments and the control simulations (non-urban–BEPurban).

Further analysis that utilizes the difference between non-urban and urban reveals negative values ranging between −0.4 K and 0 K. These values suggest an increase in temperature in the northern and western locations of the study domain, while the positive values indicate a decrease in temperature, particularly in the southern locations. This implies that higher temperatures were observed for urban areas in most northern and western locations, with the opposite trend observed in southern locations. The thermal influence appears to be limited, as contrasts in the surface temperature are relatively small in the BEPurban simulation, indicating an increase in temperature in the urban areas. Many building materials, such as concrete and asphalt, have good heat-absorption properties. This means that they absorb and retain heat from the sun, leading to higher surface temperatures and contributing to overall warming in urban areas [62–64]. Overall, the presence and characteristics of buildings in urban areas can significantly impact local temperatures, leading to higher temperatures compared to the surrounding rural areas.

3.3.4. Relative Humidity

In Figure 10, the spatial characteristics of relative humidity (RH) reveal the highest RH in western and some northern locations of the Lake Victoria basin for both the non-urban and the control simulations (BEPurban). In comparative terms, relatively larger variations were observed between BEPurban and non-urban. For instance, the differences ranged between −1 and −4 for non-urban and BEPurban, dominating central and some western locations. This indicates that the magnitude of the difference was observed to be high for non-urban and BEPurban, signifying the high-level influence of BEPurban on RH. Based on these results, this study concludes that there is generally an increase in temperature and a decrease in RH due to the effects of roughness and buildings. As temperatures rise, the air's capacity to hold moisture also increases, potentially leading to lower relative humidity levels. This effect is particularly noticeable in densely built-up areas with significant heat generation from buildings, industrial processes, and transportation. Buildings can influence local airflow patterns, potentially impacting the distribution of moisture in the air. In some cases, buildings can also obstruct natural airflow, which may affect the dispersion of moisture and lead to variations in relative humidity levels in different parts of the urban environment [65].

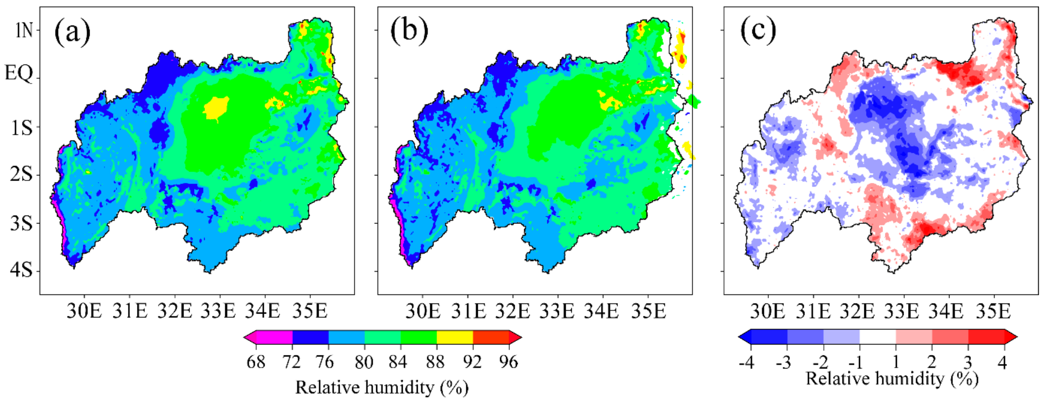

Figure 10. Spatially distributed relative humidity (RH): (**a**) non-urban and (**b**) control (BEPurban). (**c**) The difference between the non-urban and the control simulations (non-urban–BEPurban) and time series of the spatial average diurnal variation in RH over the Lake Victoria basin.

3.3.5. Sensible Heat

As shown in Figure 11, the sensible heat flux is dominated by positive fluxes (0–75 W/m^2) over the land, with a few locations showing negative fluxes. The magnitude of the difference is notable for non-urban and BEPurban, with the highest values observed over the eastern locations. For sensible heat, in the comparison between non-urban and BEPurban (hfx non-urban, hfx BEPurban), high magnitudes of negative values, indicating an increase in sensible heat flux due to urbanization, can be seen over the southern locations, while positive values (decreased sensible heat flux) are observed over the lake and western locations. An increase in surface temperatures around the buildings contributes to a higher sensible heat flux. The stored heat is then released back into the atmosphere, impacting the local heat exchange between the surface and the air [66].

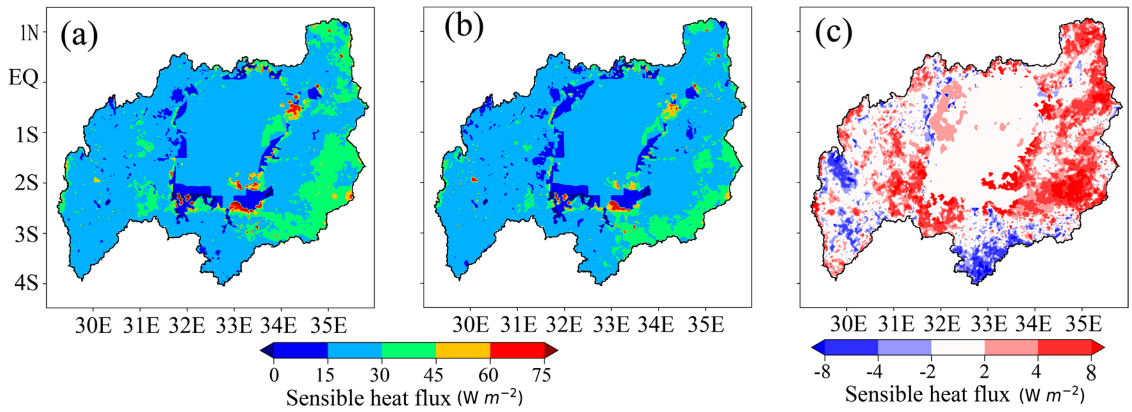

Figure 11. Spatially distributed upward sensible heat flux (hfx): (**a**) non-urban, (**b**) BEPurban, and (**c**) the difference between the non-urban experiment and the control simulation (non-urban–BEPurban).

3.3.6. Latent Heat

The latent heat flux was observed to be highest over Lake Victoria (in a, b, and c), primarily because there is less impervious coverage in the urban grid in the urban and BEPurban simulations, which promotes a greater latent heat flux due to evapotranspiration over Lake Victoria. This pattern is particularly evident in eastern locations (Figure 12). According to the model, latent heat was consistently high over the lake throughout the study period. In terms of magnitude, the disparities between urban and non-urban parametrizations seemed to have less of an impact on surface energy fluxes across the entire lake basin. However, this contrasted with the significant influence of non-urban and BEPurban parametrizations on surface energy fluxes in the same region. The presence of the buildings causes the rate of evapotranspiration to decrease, leading to a reduction in the latent heat flux. Heat retention and redistribution lead to elevated surface temperatures in urban areas, which, in turn, affect the local water cycle and can influence the availability of moisture for evaporation, potentially reducing the overall latent heat flux in the vicinity of buildings [67,68].

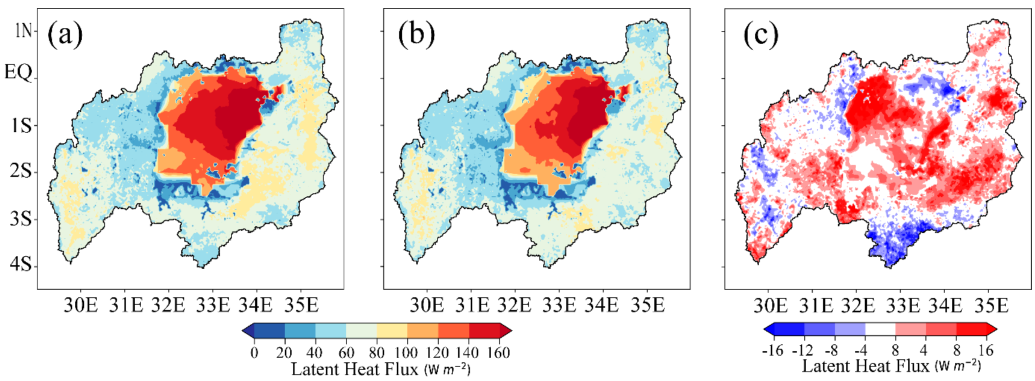

Figure 12. Spatially distributed latent heat flux (l h): (**a**) non-urban, (**b**) BEPurban, and (**c**) the difference between the non-urban and control simulations (non-urban–BEPurban) and time series of the average diurnal spatial variation across l h over the Lake Victoria basin.

3.3.7. Vertically Integrated Moisture Flux

Figure 13 shows the results for the integrated moisture flux, indicating a clear convergence of air moisture over the urban area. An increase in the moisture flux implies a rise in the amount of water vapor being transported in a specific direction. This can occur due to various atmospheric processes, including changes in atmospheric circulation patterns, temperature, and humidity gradients, or the availability of surface moisture. In regions with high levels of humidity, an elevation in the moisture flux can lead to more frequent and intense precipitation events, potentially causing flooding and landslides.

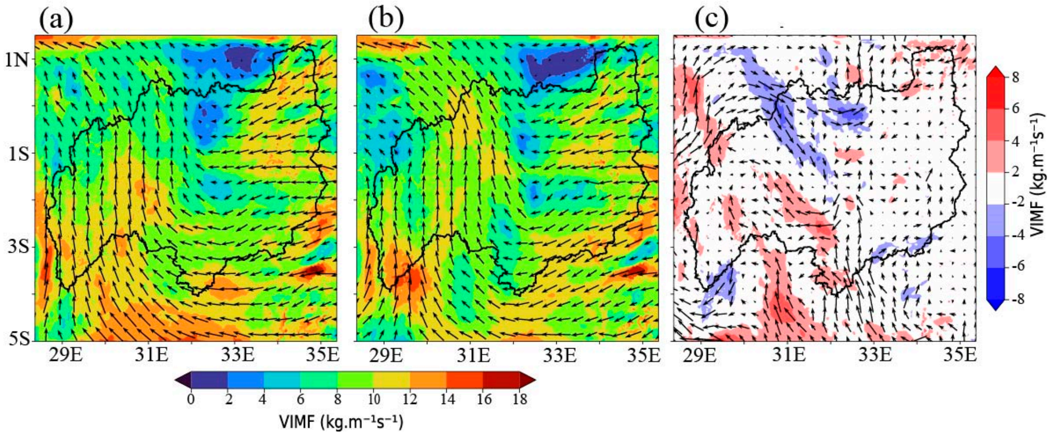

Figure 13. Vertical profiles of the integrated moisture flux (shaded, in kg $m^{-1}s^{-1}$) and horizontal wind vectors (in the u and v directions in m/s) over the storm period, where (**a**) is the non-urban, (**b**) BEPurban, and (**c**)the difference between non-urban and BEPurban.

The water vapor flux (WVF) shown in Figure 13 reveals the transportation of moisture from the southeast to the study domain, with a pronounced influence over the eastern locations. The study also observed a variation in the moisture concentration when comparing non-urban with BEP-urban (Figure 13c). BEP-urban demonstrated a more pronounced effect on moisture transportation compared to the non-urban experiment. The study noted an increase in moisture over the central locations of the study domain due to the influence of buildings, as indicated by negative values. This suggests that the urban heat island (UHI) not only enhances convergence over the urban area (due to the additional sensible heat flux) but also amplifies the land/lake temperature contrast. This contrast, in turn, reinforces the lake breeze, bringing in additional moisture. Changes in the vertical distribution of moisture due to urban development can influence local precipitation patterns. The altered moisture flux resulting from the presence of buildings can impact the formation and behavior of clouds and precipitation processes [69,70].

4. Summary and Conclusions

The study investigated the impact of the urban canopy on an extreme rainfall event in the Lake Victoria basin. Utilizing the Weather Research and Forecasting (WRF) model, three sets of experiments were conducted over three days in this East African region. The model verification, employing metrics such as the false alarm ratio (FAR), the frequency bias index (FBI), the probability of detection (POD), and the critical success index (CSI), indicates that the WRF model performed well, aligning closely with both CMORPH and ERA5 in capturing spatial patterns during the extreme event. In terms of the model's performance, the study indicates that WRF simulations effectively represent the extreme event, with BEPurban outperforming the urban experiment. Therefore, WRF can be regarded as a reliable tool for forecasting weather parameters during such extreme events.

Comparisons between the well-performing control run (BEPurban) and the non-urban run simulations, where the urban area is replaced with forest, reveal that the urban environment amplifies extreme rainfall events. The control run generates 30 mm more rainfall over the city compared to its non-urban counterpart. This enhancement is attributed to urban factors such as reduced evapotranspiration, resulting in an increased sensible heat flux (by 75 W m^2) and an elevated urban heat island effect (0.4 K increase in air surface temperature). These factors trigger horizontal convergence and enhance the sea breeze, leading to the convergence of moisture from the southern sea area over built-up areas. This creates favorable conditions for convection and rainfall processes.

Understanding the impact of the urban canopy on extreme rainfall events is crucial for policymakers and urban planners. It helps in the development of strategies to mitigate flood risks and promote sustainable urban development. The WRF model serves as a valuable tool for assessing and predicting the influences of urbanization on rainfall patterns, facilitating informed decision making amid increasing urbanization in the region. This type of research helps to improve our understanding of how urbanization affects meteorology and hydrometeorology, providing a foundation for enhancing the resilience of future cities to weather- and climate-related hazards. As far as the community is concerned, this study contributes to safeguarding the well-being of communities in the Lake Victoria basin by providing knowledge that can improve preparedness and responses to extreme rainfall events, including the implementation of early-warning systems, disaster risk reduction measures, and community-based adaptation strategies. The robustness of the validation and verification of the study using the WRF model is reduced due to the restricted availability of in situ observational data. These data are characterized by frequent gaps, limited accessibility, and high costs, and they are often less accurate due to a variety of influencing factors.

Author Contributions: Conceptualization, J.B and J.Y; methodology, A.A.S.C.; software, A.A.S.C.; validation, J.B., and J.Y.; resources, J.Y.; visualization, N.M. and E.Y.; data curation, J.B. and A.A.S.C.; writing—original draft preparation, J.B.; writing—review and editing, N.M. and E.Y.; supervision, J.Y.; project administration, J.Y.; funding acquisition, J.Y. All authors have read and agreed to the published version of the manuscript.

Funding: This research received no external funding.

Institutional Review Board Statement: Not applicable.

Informed Consent Statement: Not Applicable.

Data Availability Statement: The data presented in this study are available on request from the corresponding author. The data are not publicly available due to privacy and the data is also still being used in the thesis which is not yet complete.

Acknowledgments: The authors acknowledge the funders and providers of the different datasets used in this study. Additionally, we acknowledge and thank the Nanjing University of Information Science and Technology (NUIST) for supporting and providing the necessary resources.

Conflicts of Interest: The authors declare no conflicts of interest.

Appendix A

Appendix A.1 Statistical Equations

$$Bias = \frac{1}{n}\sum_{i=1}^{n}(m_i - O_i) \tag{A1}$$

$$Normalized\ bias = \frac{\frac{1}{n}\sum_{i=1}^{n}(m_i - O_i)}{O'} \times 100 \tag{A2}$$

$$RMSE = \sqrt{\frac{1}{n}\sum_{i=1}^{n}(m_i - O_i)^2} \tag{A3}$$

$$Normalised\ RMSE = \frac{\sqrt{\frac{1}{n}\sum_{i=1}^{n}(m_i - O_i)^2}}{O'} \times 100 \tag{A4}$$

$$R = \frac{\sum_{i=1}^{n}(m_i - m')(O_i - O')}{\sqrt{\sum_{i=1}^{n}(m_i - m')^2}\sqrt{\sum_{i=1}^{n}(O_i - O')^2}} \tag{A5}$$

$$False\ alarm\ ratio\ (FAR) = \frac{HH}{HH + FA} \tag{A6}$$

$$Frequency\ bias\ index\ (FBI) = \frac{HH + MM}{HH + FA} \tag{A7}$$

$$Probability\ of\ detection\ (POD) = \frac{HH}{HH + MM} \tag{A8}$$

$$Critical\ success\ index\ (CSI) = \frac{HH}{HH + MM + FA} \tag{A9}$$

where n is 4 days, m_i is the simulation, O_i is the observation, and m' and O' are the average values of the simulated data and observed data (ERA5 data), respectively. *HH* represents the hits, *MM* represents the missed events, and *FA* is the false alarm, as shown in the contingency table in Table 4. *FAR* indicates the grids of the WRF simulated rainfall that have no rainfall compared to the observation data grids. It ignores the misses and is sensitive to the frequency of rainfall occurrence during the event. *FBI* indicates the tendency for overestimation (*FBI* > 1) or underestimation (*FBI* < 1) of WRF simulated rainfall occurrence. *POD* indicates the grid that correctly simulated rainfall, compared to the observation grid's rainfall; it is sensitive to the frequency of rainfall occurrence during the event and ignores false alarms. *CSI* indicates how the grid rainfall simulated by WRF corresponds to the estimates based on observation data. It penalizes both misses and false alarms and is sensitive to hits; the perfect scores are 0, 1, 1, and 1, as described in more detail in [71].

Appendix A.2 Moisture-Flux Convergence Equation

$$MFC = -\int_0^{ps} \nabla P.(uq)dp/g = P - E + \frac{\partial w}{\partial t} \tag{A10}$$

where *MFC* is the horizontal moisture-flux convergence integrated from the surface to the top of the atmosphere. $\nabla P.()$ is the horizontal divergence in pressure coordinates, $u = (u, v)$ is the horizontal wind vector, q is the specific humidity, P is the precipitation rate, E is the evaporation rate, and $w = \int_0^{ps} qdp/g$ is the total precipitable water with negligible storage $\frac{\partial w}{\partial t}$. Thus, the positive (negative) values of *MFC* correspond to the positive (negative) net precipitation [23,72].

References

1. Wainwright, C.M.; Finney, D.L.; Kilavi, M.; Black, E.; Marsham, J.H. Extreme rainfall in East Africa, October 2019–January 2020 and context under future climate change. *Weather* **2021**, *76*, 26–31. [CrossRef]
2. Jacobs, L.; Maes, J.; Mertens, K.; Sekajugo, J.; Thiery, W.; van Lipzig, N.; Poesen, J.; Kervyn, M.; Dewitte, O. Reconstruction of a flash flood event through a multi-hazard approach: Focus on the Rwenzori Mountains, Uganda. *Nat. Hazards* **2016**, *84*, 851–876. [CrossRef]
3. Chen, F.; Miao, S.; Tewari, M.; Bao, J.-W.; Kusaka, H. A numerical study of interactions between surface forcing and sea breeze circulations and their effects on stagnation in the greater Houston area. *J. Geophys. Res. Atmos.* **2011**, *116*, 12. [CrossRef]
4. Liu, Y.; Chen, F.; Warner, T.; Basara, J. Verification of a Mesoscale Data-Assimilation and Forecasting System for the Oklahoma City Area during the Joint Urban 2003 Field Project. *J. Appl. Meteorol. Climatol.* **2006**, *45*, 912–929. [CrossRef]
5. Kusaka, H.; Kondo, H.; Kikegawa, Y.; Kimura, F. A Simple Single-Layer Urban Canopy Model For Atmospheric Models: Comparison With Multi-Layer And Slab Models. *Bound. Layer Meteorol.* **2001**, *101*, 329–358. [CrossRef]
6. Martilli, A.; Clappier, A.; Rotach, M.W. An urban surface exchange parameterisation for mesoscale models. *Bound. Layer Meteorol.* **2002**, *104*, 261–304. [CrossRef]
7. Salamanca, F.; Krpo, A.; Martilli, A.; Clappier, A. A new building energy model coupled with an urban canopy parameterization for urban climate simulations-part I. formulation, verification, and sensitivity analysis of the model. *Theor. Appl. Climatol.* **2010**, *99*, 331–344. [CrossRef]
8. Yang, P.; Ren, G.; Yan, P. Evidence for a Strong Association of Short-Duration Intense Rainfall with Urbanization in the Beijing Urban Area. *J. Clim.* **2017**, *30*, 5851–5870. [CrossRef]
9. Li, Y.; Fowler, H.J.; Argüeso, D.; Blenkinsop, S.; Evans, J.P.; Lenderink, G.; Yan, X.; Guerreiro, S.B.; Lewis, E.; Li, X. Strong Intensification of Hourly Rainfall Extremes by Urbanization. *Geophys. Res. Lett.* **2020**, *47*, e2020GL088758. [CrossRef]

10. Hjelmstad, A.; Shrestha, A.; Garcia, M.; Mascaro, G. Propagation of radar rainfall uncertainties into urban pluvial flood modeling during the North American monsoon. *Hydrol. Sci. J.* **2021**, *66*, 2232–2248. [CrossRef]
11. Han, J.-Y.; Baik, J.-J.; Lee, H. Urban impacts on precipitation. *Asia-Pac. J. Atmos. Sci.* **2014**, *50*, 17–30. [CrossRef]
12. Shepherd, J.M. A Review of Current Investigations of Urban-Induced Rainfall and Recommendations for the Future. 2005. Available online: http://EarthInteractions.org (accessed on 17 January 2024).
13. Debbage, N.; Shepherd, J.M. Urban influences on the spatiotemporal characteristics of runoff and precipitation during the 2009 Atlanta flood. *J. Hydrometeorol.* **2019**, *20*, 3–21. [CrossRef]
14. Roukounakis, N.; Varotsos, K.V.; Katsanos, D.; Lemesios, I.; Giannakopoulos, C.; Retalis, A. High Resolution WRF Modelling of Extreme Heat Events and Mapping of the Urban Heat Island Characteristics in Athens, Greece. *Sustainability* **2023**, *15*, 16509. [CrossRef]
15. Liu, J.; Niyogi, D. Meta-analysis of urbanization impact on rainfall modification. *Sci. Rep.* **2019**, *9*, 7301. [CrossRef] [PubMed]
16. Schwaab, J.; Meier, R.; Mussetti, G.; Seneviratne, S.; Bürgi, C.; Davin, E.L. The role of urban trees in reducing land surface temperatures in European cities. *Nat. Commun.* **2021**, *12*, 6763. [CrossRef]
17. Wu, W.; Ren, L.; Wei, Y.; Guo, M. Impacts of Urbanization on Extreme Regional Precipitation Events. *Discret. Dyn. Nat. Soc.* **2021**, *2021*, 2210184. [CrossRef]
18. Zhang, L.; Yang, L.; Zohner, C.M.; Crowther, T.W.; Li, M.; Shen, F.; Guo, M.; Qin, J.; Yao, L.; Zhou, C. Direct and indirect impacts of urbanization on vegetation growth across the world's cities. *Sci. Adv.* **2023**, *8*, eabo0095. [CrossRef] [PubMed]
19. Droste, A.M.; Steeneveld, G.J.; Holtslag, A.A.M. Introducing the urban wind island effect. *Environ. Res. Lett.* **2018**, *13*, 094007. [CrossRef]
20. Li, Q.; Yang, J.; Yang, L. Impact of Urban Roughness Representation on Regional Hydrometeorology: An Idealized Study. *J. Geophys. Res. Atmos.* **2021**, *126*, e2020JD033812. [CrossRef]
21. Rajeswari, J.R.; Srinivas, C.V.; Yesubabu, V.; Prasad, D.H.; Venkatraman, B. Impacts of Urbanization, Aerodynamic Roughness, and Land Surface Processes on the Extreme Heavy Rainfall Over Chennai, India. *J. Geophys. Res. Atmos.* **2021**, *126*, e2020JD034017. [CrossRef]
22. Jonescu, E.E.; Ramanayaka, C.E.; Olatunji, O.; Jonescu, E.E.; Olatunji, O.A. How Urban Heat Islands Effect Crime: Understanding the Implications of Temperature, Population Density, and Green Canopy Cover in Shaping Built Environments. *Qeios* **2023**. [CrossRef]
23. Fowler, H.J.; Lenderink, G.; Prein, A.F.; Westra, S.; Allan, R.P.; Ban, N.; Barbero, R.; Berg, P.; Blenkinsop, S.; Do, H.X.; et al. Anthropogenic intensification of short-duration rainfall extremes. *Nat. Rev. Earth Environ.* **2021**, *2*, 107–122. [CrossRef]
24. Mbeche, O.O. Accessibility Modeling for a Developing Economy: The Case of Inter-Regional Traffic Flow in the Lake Victoria Basin, Kenya. *J. Civ. Eng. Res. Pract.* **2004**, *1*, 89–101. [CrossRef]
25. Kanyari, P.W.N.; Kagira, J.M.; Mhoma, J.R.L. Prevalence of endoparasites in cattle within urban and peri-urban areas of Lake Victoria Basin, Kenya with special reference to zoonotic potential. *Sci. Parasitol.* **2020**, *11*, 171–178.
26. Onyutha, C.; Willems, P. Uncertainty in calibrating generalised Pareto distribution to rainfall extremes in Lake Victoria basin. *Hydrol. Res.* **2015**, *46*, 356. [CrossRef]
27. Mugo, R.; Waswa, R.; Nyaga, J.W.; Ndubi, A.; Adams, E.C.; Flores-Anderson, A.I. Quantifying land use land cover changes in the lake victoria basin using satellite remote sensing: The trends and drivers between 1985 and 2014. *Remote Sens.* **2020**, *12*, 2829. [CrossRef]
28. Semazzi, F.H.M. Framework for climate services in developing countries. *Clim Res.* **2015**, *47*, 145–150. [CrossRef]
29. Kusaka, H.; Kimura, F. Coupling a single-layer urban canopy model with a simple atmospheric model: Impact on urban heat island simulation for an idealized case. *J. Meteorol. Soc. Jpn.* **2004**, *82*, 67–80. [CrossRef]
30. Brunner, M.I.; Swain, D.L.; Wood, R.R.; Willkofer, F.; Done, J.M.; Gilleland, E.; Ludwig, R. An extremeness threshold determines the regional response of floods to changes in rainfall extremes. *Commun. Earth Environ.* **2021**, *2*, 173. [CrossRef]
31. Thiery, W.; Davin, E.L.; Seneviratne, S.I.; Bedka, K.; Lhermitte, S.; Van Lipzig, N.P.M. Hazardous thunderstorm intensification over Lake Victoria. *Nat. Commun.* **2016**, *7*, 12786. [CrossRef]
32. Wang, J.; Xue, P.; Pringle, W.; Yang, Z.; Qian, Y. Impacts of Lake Surface Temperature on the Summer Climate Over the Great Lakes Region. *J. Geophys. Res. Atmos.* **2022**, *127*, e2021JD036231. Available online: https://api.semanticscholar.org/CorpusID:248877388 (accessed on 17 January 2024). [CrossRef]
33. Sun, X. An Investigation of the Role of Lake Surface Temperature on Precipitation Over Lake Victoria Basin using a Limited-area Numerical Model ! ! by. 2014. Available online: https://api.semanticscholar.org/CorpusID:73619206 (accessed on 17 January 2024).
34. Yang, S.; Ran, G.; Zhang, W.; Wang, Z.H. The Cooling Effect of an Urban Lake Landscape on the Urban Heat Island: A Case Study in Jinan, China. *Appl. Ecol. Environ. Res.* **2020**, *18*, 2197–2211. Available online: https://api.semanticscholar.org/CorpusID:226508998 (accessed on 17 January 2024). [CrossRef]
35. Skamarock, C.; Klemp, B.; Dudhia, J.; Gill, O.; Liu, Z.; Bemer, J.; Wang, W.; Powers, G.; Duda, G.; Barker, D.; et al. A Description of the Advanced Research WRF Model Version 4. 2019. Available online: https://api.semanticscholar.org/CorpusID:196211930 (accessed on 17 January 2024).
36. Bougeault, P.; Lacarrere, P. Parameterization of Orography-Induced Turbulence in a Mesobeta—Scale Model. *Mon. Weather Rev.* **1989**, *117*, 1872–1890. [CrossRef]

37. Wang, W.; Tewari, M.; Chen, F.; Dudhia, J.; Lemone, M.A.; Mitchell, K.; Ek, M.; Gayno, G.; Wegiel, G.; Cuenca, R. Implementation and Verification of the United NOAH Land Surface Model in the WRF Model NASA AirMOSS View Project Regional Integrated Hydrology and Earth System Modeling View Project Mukul Tewari. 942. Available online: https://www.researchgate.net/publication/286272692 (accessed on 17 January 2024).
38. Iacono, M.J. *Final Technical Report For the Project: Application of Improved Radiation Modeling to General Circulation Models*; Atmospheric and Environmental Research, Inc.: Lexington, MA, USA, 2003.
39. Jiménez, P.A.; Dudhia, J.; González-Rouco, J.F.; Navarro, J.; Montávez, J.P.; García-Bustamante, E. A revised scheme for the WRF surface layer formulation. *Mon. Weather Rev.* **2012**, *140*, 898–918. [CrossRef]
40. Zhao, X.; Lin, Y.; Luo, Y.; Qian, Q.; Liu, X.; Liu, X.; Colle, B.A. A Double-Moment SBU-YLIN Cloud Microphysics Scheme and Its Impact on a Squall Line Simulation. *J. Adv. Model Earth Syst.* **2021**, *13*, e2021MS002545. [CrossRef]
41. Ronald, O.; Meteorology, B. Makerere University Examining Observed and Simulated Extreme Rainfall Events over Lake Victoria Basin in Uganda. Master's Thesis, Makerere University, Kampala, Uganda, 2019.
42. Joyce, R.J.; Janowiak, J.E.; Arkin, P.A.; Xie, P. CMORPH: A Method that Produces Global Precipitation Estimates from Passive Microwave and Infrared Data at High Spatial and Temporal Resolution. *J. Hydrometeorol.* **2004**, *5*, 487–503. [CrossRef]
43. Xie, P.; Joyce, R.; Wu, S.; Yoo, S.-H.; Yarosh, Y.; Sun, F.; Lin, R. Reprocessed, bias-corrected CMORPH global high-resolution precipitation estimates from 1998. *J. Hydrometeorol.* **2017**, *18*, 1617–1641. [CrossRef]
44. Wang, J.; Chen, F.; Van Doan, Q.; Xu, Y. Exploring the effect of urbanization on hourly extreme rainfall over Yangtze River Delta of China. *Urban Clim.* **2021**, *36*, 100781. [CrossRef]
45. Zhong, S.; Yang, X.Q. Ensemble simulations of the urban effect on a summer rainfall event in the Great Beijing Metropolitan Area. *Atmos. Res.* **2015**, *153*, 318–334. [CrossRef]
46. Van Doan, Q.; Kobayashi, S.; Kusaka, H.; Chen, F.; He, C.; Niyogi, D. Tracking Urban Footprint on Extreme Precipitation in an African Megacity. *J. Appl. Meteorol. Climatol.* **2023**, *62*, 209–226. [CrossRef]
47. Dee, D.P.; Uppala, S.M.; Simmons, A.J.; Berrisford, P.; Poli, P.; Kobayashi, S.; Andrae, U.; Balmaseda, M.A.; Balsamo, G.; Bauer, P.; et al. The ERA-Interim reanalysis: Configuration and performance of the data assimilation system. *Q. J. R. Meteorol. Soc.* **2011**, *137*, 553–597. [CrossRef]
48. Hersbach, H.; Bell, B.; Berrisford, P.; Hirahara, S.; Horányi, A.; Muñoz-Sabater, J.; Nicolas, J.; Peubey, C.; Radu, R.; Schepers, D.; et al. The ERA5 global reanalysis. *Q. J. R. Meteorol. Soc.* **2020**, *146*, 1999–2049. [CrossRef]
49. Kalnay, E.; Cai, M. Impact of urbanization and land-use change on climate. *Nature* **2003**, *423*, 528–531. [CrossRef]
50. Wang, J.; Yan, Z.-W. Urbanization-related warming in local temperature records: A review. *Atmos. Ocean. Sci. Lett.* **2016**, *9*, 129–138. [CrossRef]
51. Wang, J.; Yan, Z.; Jones, P.D.; Xia, J. On 'observation minus reanalysis' method: A view from multidecadal variability. *J. Geophys. Res. Atmos.* **2013**, *118*, 7450–7458. [CrossRef]
52. Mohammed, Y.; Salman, A.S. Effect of Urban Geometry and Green Area on the Formation of the Urban Heat Island in Baghdad City. 2018. Available online: https://api.semanticscholar.org/CorpusID:54692140 (accessed on 19 January 2024).
53. Earl, N.; Simmonds, I.; Tapper, N. Weekly cycles in peak time temperatures and urban heat island intensity. *Environ. Res. Lett.* **2016**, *11*, 074003. Available online: https://api.semanticscholar.org/CorpusID:73703571 (accessed on 19 January 2024). [CrossRef]
54. Humaida, N.; Saputra, M.H.; Sutomo; Hadiyan, Y. Urban gardening for mitigating heat island effect. *IOP Conf. Ser. Earth Environ. Sci.* **2023**, *1133*, 012048. Available online: https://api.semanticscholar.org/CorpusID:256053242 (accessed on 19 January 2024). [CrossRef]
55. Lamontagne, J.R.; Barber, C.A.; Vogel, R.M. Improved Estimators of Model Performance Efficiency for Skewed Hydrologic Data. *Water Resour. Res.* **2020**, *56*, e2020WR027101. [CrossRef]
56. Stensrud, D.J.; Skindlov, J.A. Gridpoint Predictions of High Temperature from a Mesoscale Model. *Weather. Forecast.* **1996**, *11*, 103–110. Available online: https://api.semanticscholar.org/CorpusID:123092537 (accessed on 19 January 2024). [CrossRef]
57. Csébfalvi, A. Critical Investigation of the Combined Compliance Average and Spreading Measures in the Robust Topology Optimization with Uncertain Loading Magnitude and Direction. *Period. Polytech. -Civ. Eng.* **2020**, *64*, 1275–1283. Available online: https://api.semanticscholar.org/CorpusID:222453863 (accessed on 19 January 2024). [CrossRef]
58. Kutlugün, M.A.; Sirin, Y. Reducing false positive rate with the help of scene change indicator in deep learning based real-time face recognition systems. *Multimed. Tools Appl.* **2023**, *82*, 47517–47536. Available online: https://api.semanticscholar.org/CorpusID:258684831 (accessed on 19 January 2024). [CrossRef] [PubMed]
59. Tsoka, S.; Velikou, K.; Tolika, K.; Tsikaloudaki, A. Evaluating the combined effect of climate change and urban microclimate on buildings' heating and cooling energy demand in a mediterranean city. *Energies* **2021**, *14*, 5799. [CrossRef]
60. Khalaim, O.; Zabarna, O.; Kazantsev, T.; Panas, I.; Polishchuk, O. Urban green infrastructure inventory as a key prerequisite to sustainable cities in Ukraine under extreme heat events. *Sustainability* **2021**, *13*, 2470. [CrossRef]
61. Pereira, L.D.; Saraiva, N.B.; Soares, N. Hygrothermal Behavior of Cultural Heritage Buildings and Climate Change: Status and Main Challenges. *Appl. Sci.* **2023**, *13*, 3445. [CrossRef]
62. Le, M.T.; Le, H.T.; Shukurov, I.; Slesarev, M. Sulfur-extended asphalt concrete with assessing the surface temperature of roads affecting urban heat island. *IOP Conf. Ser. Mater. Sci. Eng.* **2020**, *869*, 225614376. Available online: https://api.semanticscholar.org/CorpusID:225614376 (accessed on 19 January 2024). [CrossRef]

63. Ziaeemehr, B.; Jandaghian, Z.; Ge, H.; Lacasse, M.; Moore, T. Increasing Solar Reflectivity of Building Envelope Materials to Mitigate Urban Heat Islands: State-of-the-Art. *Rev. Build.* **2023**, *13*, 2868. Available online: https://api.semanticscholar.org/CorpusID:265272152 (accessed on 19 January 2024).
64. MWasik; Dereszewski, A.; Łapka, P. Prototype of an experimental stand for investigating heat and moisture transfer phenomena in building materials. *J. Phys. Conf. Ser.* **2023**, *2423*, 256023745. Available online: https://api.semanticscholar.org/CorpusID:256023745 (accessed on 19 January 2024).
65. Liang, Q.; Miao, Y.; Zhang, G.; Liu, S. Simulating Microscale Urban Airflow and Pollutant Distributions Based on Computational Fluid Dynamics Model: A Review. *Toxics* **2023**, *11*, 265164843. Available online: https://api.semanticscholar.org/CorpusID:265164843 (accessed on 19 January 2024).
66. Pokas, R.; Sirvydas, A.; Kulkovas, V.; Poskas, P.; Jouhara, H.; Miliauskas, G.; Puida, E. Flue Gas Condensation in a Model of the Heat Exchanger: The Effect of the Cooling Water Flow Rate and Its Temperature on Local Heat Transfer. *Appl. Sci.* **2022**, 254613251. Available online: https://api.semanticscholar.org/CorpusID:254613251 (accessed on 19 January 2024).
67. Yang, L.; Yu, K.; Ai, J.; Liu, Y.; Yang, W.; Liu, J. Dominant Factors and Spatial Heterogeneity of Land Surface Temperatures in Urban Areas: A Case Study in Fuzhou, China. *Remote Sens.* **2022**, *14*, 1266. Available online: https://api.semanticscholar.org/CorpusID:247300801 (accessed on 19 January 2024).
68. Bateman, H.L.; Allen, B.D.; Moore, M.S.; Hondula, D.M. Urban heat and desert wildlife: Rodent body condition across a gradient of surface temperatures. *Urban Ecosyst.* **2023**, *26*, 917–928. Available online: https://api.semanticscholar.org/CorpusID:258086083 (accessed on 19 January 2024). [CrossRef]
69. He, L.; Li, Q.; Wang, Y.; Lee, J.H.W.; Xu, Y.; Li, G. Effects of Urban Expansion and Anthropogenic Heat Enhancement on Tropical Cyclone Precipitation in the Greater Bay Area of China. *J. Geophys. Res. Atmos.* **2023**, *128*, 260528201. Available online: https://api.semanticscholar.org/CorpusID:260528201 (accessed on 19 January 2024). [CrossRef]
70. Huang, X.; Song, J. Urban moisture and dry islands: Spatiotemporal variation patterns and mechanisms of urban air humidity changes across the globe. *Environ. Res. Lett.* **2023**, *18*, 103003. Available online: https://api.semanticscholar.org/CorpusID:261646381 (accessed on 19 January 2024). [CrossRef]
71. Umer, Y.; Ettema, J.; Jetten, V.; Steeneveld, G.J.; Ronda, R. Evaluation of the wrf model to simulate a high-intensity rainfall event over kampala, uganda. *Water* **2021**, *13*, 873. [CrossRef]
72. Siler, N.; Bonan, D.B.; Donohoe, A. Diagnosing Mechanisms of Hydrologic Change under Global Warming in the CESM1 Large Ensemble. *J. Clim.* **2023**, *36*, 8243–8257. [CrossRef]